Cloud Sky Cover versus Cloud Fraction: Whole-Sky Simulations and Observations

EVGUENI KASSIANOV, CHARLES N. LONG, AND MIKHAIL OVTCHINNIKOV

Pacific Northwest National Laboratory, Richland, Washington

(Manuscript received 3 December 2003, in final form 1 July 2004)

ABSTRACT

The relationship between hemispherical sky cover and nadir-view cloud fraction is examined by using both model simulations and surface observations. Monte Carlo simulations of ground-based hemispherical measurements are based on four-dimensional cloud fields produced by a large-eddy simulation model. Surface hemispherical observations are performed during the Atmospheric Radiation Measurement Program's Cloudiness Intercomparison Intensive Operational Period. It is shown that (i) 15-min averages of frequently sampled (30 s) sky cover provide a reasonable estimation of the cloud fraction for limited fields of view and that (ii) this estimation can be substantially improved (for cumulus clouds) if additional information about the cloud aspect ratio is incorporated into the retrieval process.

1. Introduction

Clouds cover a significant portion of the globe (Hahn et al. 2001) and strongly influence the earth's energy budget (Harshvardhan et al. 1989). The diversity of the forms of clouds and their strong spatial and temporal variability determine the dynamics of the radiation budget to a significant degree. Knowledge of such variability is required to develop and test cloud parameterizations in numerical models of the general circulation of the atmosphere, weather forecasting, and the dynamics of clouds (Morcrette 1991; Hogan et al. 2001). Parameterization of the cloud fraction is of particular importance in calculating a radiation budget. For example, a 4% increase in the area of the globe covered by marine stratocumulus clouds would offset the predicted 2–3-K rise in global temperature due to a doubling of atmospheric carbon dioxide (Randall et al. 1984).

Estimating the cloud fraction in a partially cloudy area (grid box) is a long-standing problem. Commonly, this estimation is based on observations from satellites (Minnis 1989; Rossow et al. 1993), aircraft (Wood and Field 2000; Rodts et al. 2003) and ground-based instruments (Fairall and Hare 1990; Clothiaux et al. 1999; Pfister et al. 2003). Each observational method has advantages and disadvantages. For instance, satellite observations are still the best approach for estimating global cloud coverage, but their spatial–temporal resolution is relatively low in comparison with ground-based measurements). Moreover, observational methods and climate models use different definitions of cloud fraction. For example, the International Satellite Cloud Climatology Project (ISCCP) applies the term total cloud amount to "the fraction of the earth's surface covered by cloud" (Hahn et al. 2001). In surface climatology studies, this term is defined as "the fraction of hemispherical sky covered by cloud" (Hahn et al. 2001). Climate models, on the other hand, typically interpret the cloud fraction as "the horizontal area fraction covered by clouds as viewed from nadir" (Del Genio et al. 1996).

Currently, ground-based active remote sensing instruments are used successfully to derive cloud properties (e.g., Clothiaux et al. 2000; Lazarus et al. 2000; Mace and Benson-Troth 2002). These instruments have a narrow field of view (FOV) and detect clouds that occur directly above them. As a result, the cloud statistics obtained from such height–time transects (along wind direction) may not be representative of a larger area surrounding these instruments (e.g., Barker 1996; Berg and Stull 2002). For example, the cloud rows aligned to the wind can be organized (e.g., Christian and Wakimoto 1989). In this case, the ground-based zenith-pointing instruments with a narrow FOV observe mainly clouds or clear sky according to the relative position of these instruments to the cloud rows.

The surface radiation budget network (SURFRAD) and the Atmospheric Radiation Measurement (ARM) Program (see information online http://www.arm.gov) use total sky imagers (TSIs). These ground-based instruments have a hemispherical FOV and provide time series of fractional sky cover, N_{hemisph}. Since only the nadir-view cloud fraction, N_{nadir}, is directly applicable

Corresponding author address: Dr. Evgueni I. Kassianov, Pacific Northwest National Laboratory, 902 Battelle Blvd., P.O. Box 999, Richland, WA 99352.
E-mail: Evgueni.Kassianov@pnl.gov

to climate studies and radiation calculations, there is an essential need to establish the relationship between N_{nadir} and N_{hemisph}. In this paper, we demonstrate how accurately N_{nadir} can be estimated from hemispherical TSI observations. To address this issue, we use the results of a large eddy simulation (LES) model and surface observations during the ARM Cloudiness Intercomparison Intensive Operational Period (IOP).

In section 2 of this paper, we illustrate the main differences between N_{nadir} and N_{hemisph}. Simple cloud models that allow one to get analytical relations are applied. Section 3 provides the approach and a detailed comparison of N_{nadir} and N_{hemisph} by using four-dimensional cloud fields from the LES model. TSI observations are simulated by the Monte Carlo method. A possible correction of N_{hemisph} is discussed in section 4. Section 5 extends the N_{hemisph} analysis using surface observations during the ARM Cloudiness Intercomparison IOP. In section 6, we present a summary and conclusions.

2. Nadir-view cloud fraction and fractional sky cover

Let us consider a TSI located at the surface. We assume that this instrument has a FOV with the cone zenith angle 2α. Also we assume that a single cloud layer with cloud-base height, H_b, is located above this TSI, and the cloud-base height does not change significantly within the FOV. Projection of the FOV onto the horizontal surface at height H_b gives a circle with a radius of $R(\alpha)$. The radius $R(\alpha)$ is connected to the cone zenith angle α and H_b as $R(\alpha) = H_b \tan(\alpha)$. The cone zenith angle α is variable and can change from 0 to the maximum value α^*, where $\alpha^* = 80°$.

For a given FOV, we compare the nadir-view cloud fraction $N_{\text{nadir}}(\alpha)$ and the fractional sky cover $N_{\text{hemisph}}(\alpha)$.

- The nadir-view *cloud fraction* $N_{\text{nadir}}(\alpha)$ is defined as a ratio,

$$N_{\text{nadir}}(\alpha) = \frac{S_{\text{cld,nadir}}(\alpha)}{S_{\text{nadir}}(\alpha)}, \tag{1}$$

  where $S_{\text{cld,nadir}}(\alpha)$ is a horizontal cloud area as viewed from the *nadir* [within the circle with a radius of $R(\alpha)$]; $S_{\text{nadir}}(\alpha) = \pi R^2(\alpha)$ is the total area of this circle. Thus, $N_{\text{nadir}}(\alpha)$ is simply the fraction of the total projected area that is occupied by clouds. Both $S_{\text{cld,nadir}}(\alpha)$ and $S_{\text{nadir}}(\alpha)$ have dimensions of the area (e.g., km^2).
- The fractional *sky cover* $N_{\text{hemisph}}(\alpha)$ is defined as a ratio,

$$N_{\text{hemisph}}(\alpha) = \frac{S_{\text{cld, hemisph}}(\alpha)}{S_{\text{hemisph}}(\alpha)}, \tag{2}$$

where $S_{\text{hemisph}}(\alpha)$ is the observed solid angle with cone zenith angle 2α (as viewed by a surface observer):

$$S_{\text{hemisph}}(\alpha) = \int_0^{2\pi} d\phi \int_0^{\alpha} \sin\theta \, d\theta = 2\pi(1 - \cos\alpha), \tag{3}$$

and $S_{\text{cld,hemisph}}(\alpha)$ is the fraction of this solid angle filled by clouds. In contrast to $S_{\text{cld,nadir}}(\alpha)$ and $S_{\text{nadir}}(\alpha)$, the dimensions of $S_{\text{cld,hemisph}}(\alpha)$ and $S_{\text{hemisph}}(\alpha)$ are the steradian.

The next simple example illustrates the differences between cloud fraction N_{nadir} and sky cover N_{hemisph}. Let us consider a single cloud located within the FOV [within the circle with a radius of $R(\alpha^*)$]. This cloud has the shape of a cylinder with a variable radius R_{cld}. The cloud thickness is small relative to the cloud radius, and therefore the cylinder can be considered to be a circle with a variable radius R_{cld}. For simplicity, we assume that the centers of these two circles [with radii of $R(\alpha^*)$ and R_{cld}] coincide, and $R_{\text{cld}}(\theta) = H_b \tan(\theta)$, where $\theta \le \alpha^*$. From Eqs. (1) and (2) follows that

$$N_{\text{nadir}}(\alpha^*) = \frac{\pi R_{\text{cld}}^2(\theta)}{\pi R^2(\alpha^*)} = \frac{\tan^2(\theta)}{\tan^2(\alpha^*)} \tag{4}$$

and

$$N_{\text{hemisph}}(\alpha^*) = \frac{2\pi(1 - \cos\theta)}{2\pi(1 - \cos\alpha^*)} = \frac{1 - \cos\theta}{1 - \cos\alpha^*}. \tag{5}$$

Figure 1a shows $N_{\text{nadir}}(\alpha^*)$ and $N_{\text{hemisph}}(\alpha^*)$ as functions of the cone zenith angle θ [or cloud size $R_{\text{cld}}(\theta)$]. It is seen that $N_{\text{hemisph}}(\alpha^*)$ is substantially larger than $N_{\text{nadir}}(\alpha^*)$ if a small/intermediate cloud is located in the center of the FOV.

It can be demonstrated easily that the opposite [$N_{\text{hemisph}}(\alpha^*) < N_{\text{nadir}}(\alpha^*)$] is true when a cloud (or its parts) is located near the edge of the FOV. Assume that the cloud has a shape of an annulus, and that the centers of the circle and the annulus are the same. The annulus has a constant outer radius $R(\alpha^*)$ and variable inner radius $R(\theta)$, where $\theta \le \alpha^*$; the annulus thickness is small relative to the cloud radius. In this case,

$$N_{\text{nadir}}(\alpha^*) = 1 - \frac{\tan^2(\theta)}{\tan^2(\alpha^*)} \tag{6}$$

and

$$N_{\text{hemisph}}(\alpha^*) = 1 - \frac{1 - \cos\theta}{1 - \cos\alpha^*}. \tag{7}$$

Figure 1b demonstrates that $N_{\text{hemisph}}(\alpha^*) \ll N_{\text{nadir}}(\alpha^*)$ when the cloud covers an area near the edge of the FOV, that is, θ, is large. Note that for any given cloud size, $N_{\text{nadir}}(\alpha^*)$ is independent of the cloud position

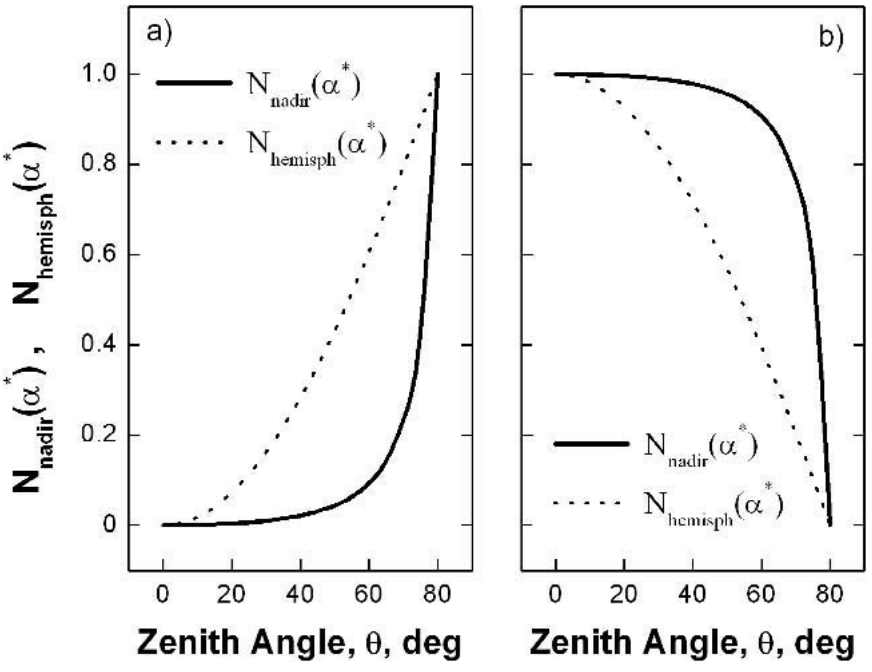

FIG. 1. Ratios $N_{\text{nadir}}(\alpha^*)$ and $N_{\text{hemisph}}(\alpha^*)$ as functions of the cone zenith angle θ, which are obtained from (a) Eqs. (4) and (5) and (b) Eqs. (6) and (7).

within the circle with a radius of $R(\alpha^*)$. In contrast, $N_{\text{hemisph}}(\alpha^*)$ can be sensitive to the cloud location.

Here we consider the simplest case only because (i) the cloud has negligible vertical extent; (ii) the cloud shape is unrealistic, very simple, and static; and (iii) the cloud does not move. Real cloud fields contain three-dimensional (3D) clouds with irregular and complex geometry, which is time dependent. Since cloud fields often move across the FOV during observations, the difference between the cloud fraction N_{nadir} and the sky cover N_{hemisph} may vary in magnitude and sign. As a result, time-averaged values of N_{nadir} and N_{hemisph} could be closely related for some FOV. To verify this hypothesis, we use a four-dimensional (three spatial and one temporal) cloud field provided by an LES model.

3. LES cloud field analysis

To estimate the requested domain size for our simulations, we use data from the ARM Cloudiness Intercomparison IOP (section 5). In particular, we apply typical values of the wind speed (υ) in a boundary layer and decorrelation length (t) of autocorrelation function of sky cover: $t \sim 15$ min and $\upsilon \sim 10$ m s^{-1} (section 5). From these values, we can assess the characteristic distance (s) of a cloud advected over the ground-based instrument: $s \sim 10$ km. Thus, our LES simulations are performed for the domain $10 \times 10 \times 2$ km^3 with 0.1-km horizontal and 0.033-km vertical resolution. Temperature and moisture profiles from soundings at the ARM Nauru site are used as input to the LES simulations. The output of this simulation is a temporal sequence of 3D cloud fields at 3-min intervals.

First we estimate the sensitivity of $N_{\text{nadir}}(\alpha)$ and $N_{\text{hemisph}}(\alpha)$ to the cloud field evolution. We obtain two sets of four-dimensional cloud fields by using LES simulation data (Fig. 2). The first set captures the cloud field motion only; that is, Taylor's frozen flow hypothesis is applied. The second set captures both individual cloud evolution and cloud field motion. These two sets are used as input to Monte Carlo simulations of TSI measurements. The Monte Carlo results obtained for the second set are considered to be the reference.

Within a 15-min time window, the geometry of individual clouds can change significantly (Fig. 3), but these geometrical changes have only a slight effect on the domain-averaged cloud fraction $N_{\text{nadir,avr}}$ (variations of $N_{\text{nadir,avr}}$ are ~10%). For Monte Carlo simulations, we assume that the cloud field moves in the y direction (wind direction) with the mean wind speed of 10 m s^{-1}, and the averaging period (temporal sample size) is 15 min. We perform the Monte Carlo simulations by assuming periodical boundary conditions in the horizontal dimensions (x and y directions).

We calculate cloud fraction $N_{\text{nadir}}(\alpha)$ and sky cover $N_{\text{hemisph}}(\alpha)$ for three different cross sections of cloud fields (in the y direction). Cross sections 1, 2, and 3 correspond to $x = 1.6$, $x = 5$, and $x = 8.6$ km, respectively. These cross sections have been chosen to represent small, mean (close to domain averaged), and large values of $N_{\text{nadir}}(0)$. Since the domain-averaged cloud fraction is almost time independent (Fig. 3), the time-

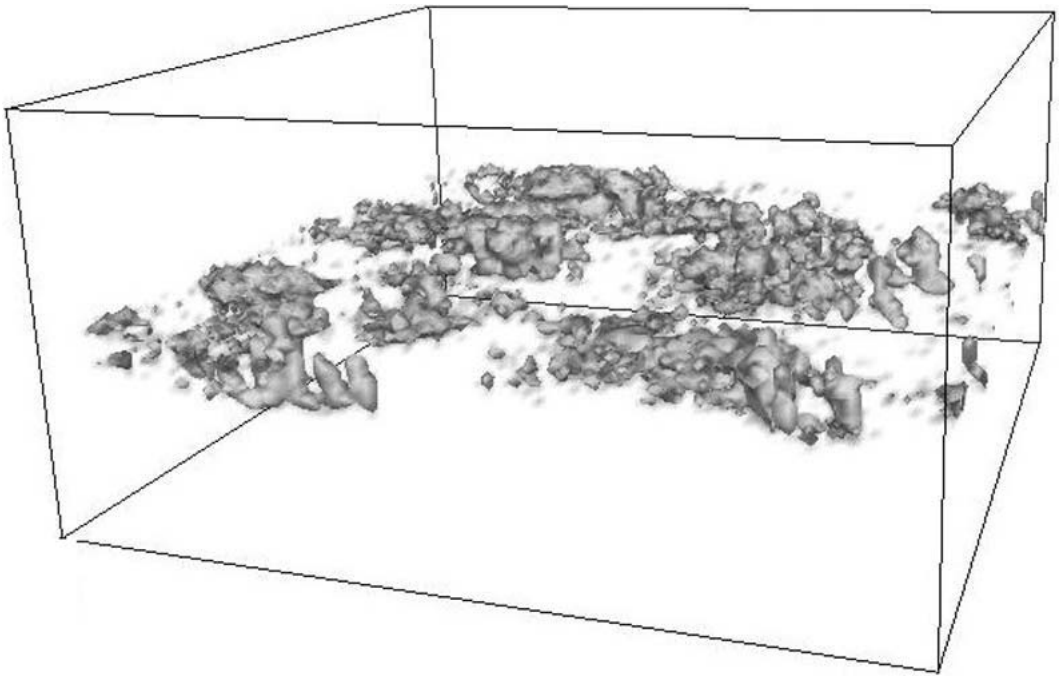

FIG. 2. One of the 3D cloud fields generated by the LES model.

averaged (15-min sample) properties $N_{\text{nadir}}(\alpha)$ and $N_{\text{hemisph}}(\alpha)$ are not sensitive to the cloud evolution (Fig. 4). Therefore, hereinafter we will consider results that are obtained for cloud field motion only. Note that $N_{\text{nadir}}(0)$ and $N_{\text{hemisph}}(0)$ are equal and represent zenith-pointing ($\alpha = 0$) observations (such as lidar or radar measurements). It is evident that $N_{\text{nadir}}(0)$ values depend strongly on the cross section and can differ substantially from $N_{\text{nadir,avr}} \sim 0.28$ (Figs. 4a,b). For example, $N_{\text{nadir}}(0)$ obtained for cross section 3 is nearly twice as large as $N_{\text{nadir,avr}}$, which means that the zenith-pointing observations can significantly (more than 2

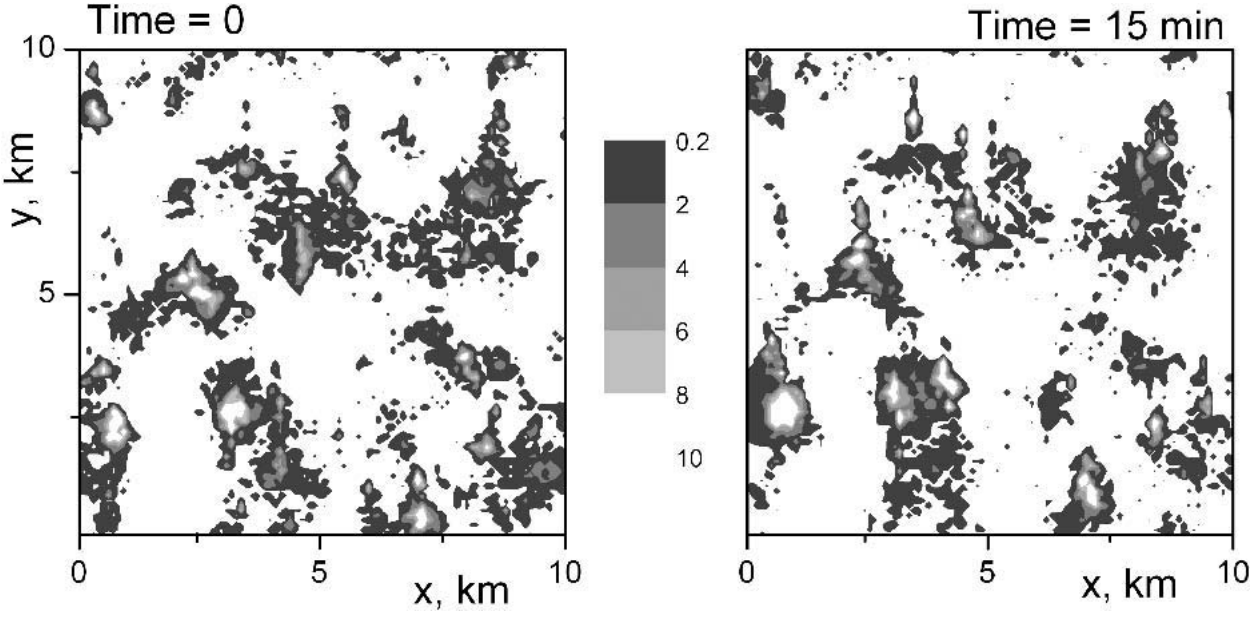

FIG. 3. LES simulation. Horizontal distribution of cloud optical depth for different instants of time *T:* (a) $T = 0$ and (b) $T = 15$ min.

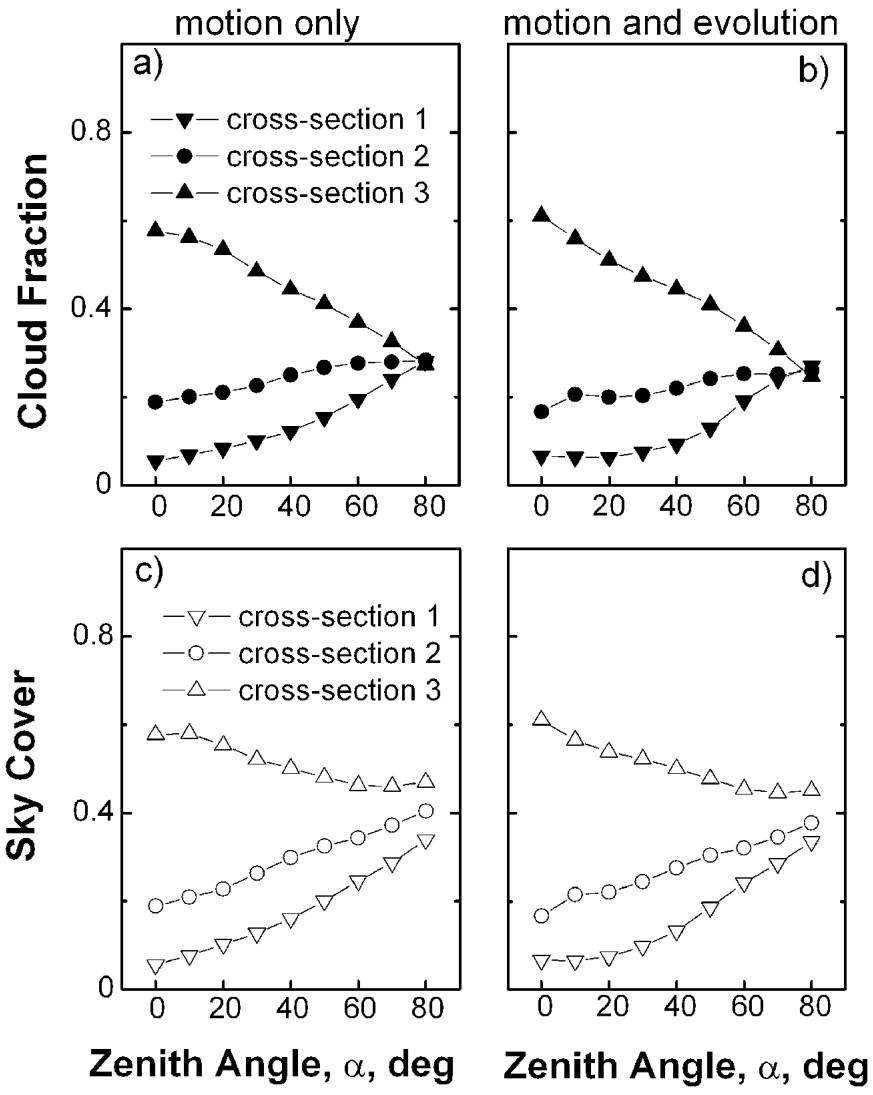

FIG. 4. Nadir-view (a), (b) cloud fraction and (c), (d) fractional sky cover as functions of the cone zenith angle α, which are obtained for two sets of cloud fields generated by LES simulation: (a), (c) first set (motion of cloud field only) and (b), (d) second set (motion and evolution of clouds).

times) overestimate or underestimate the real cloud fraction for the domain $\sim 10 \times 10$ km^2.

To accurately estimate the domain-averaged (2D) cloud fraction from zenith-pointing observations, one needs to use a large number of 1D measurements of cloud fraction in random directions [or a large number of random lines; Russ (1986)]; random lines simulation is discussed in Stoyan and Stoyan (1994). However, in practice, only a single estimation of 1D cloud fraction (along wind direction) is available. What is the probability that a 1D cloud fraction obtained from any single observation will accurately represent the 2D (domain-averaged) cloud fraction $N_{\text{nadir,avr}}$?

To estimate this probability, we consider a 2D domain ($\sim 10 \times 10$ km^2) from Fig. 3a and perform the following steps. First, we estimate the cloud fraction $N_{\text{nadir}}(0)$ for each column (x position) as a time average (along the y direction) of this 2D domain. If we assume that wind speed along the y direction is ~ 10 m s^{-1}, then a 1D cloud fraction estimation corresponds roughly to a 15-min time window. We obtain a 1D cloud fraction (from 100 cross sections along the y axis) as a function of the x coordinate (Fig. 5a). Second, we plot the corresponding histogram (Fig. 5b). Finally, we define the number of line "observations" that provide values of the 1D cloud fraction falling within an interval [0.265; 0.305]. The latter represents values of a 1D cloud fraction that differs from the "true" 2D cloud fraction $N_{\text{nadir,avr}}$ by $\sim 10\%$. The number of these "representative" 1D lines is 13, while the total number of all con-

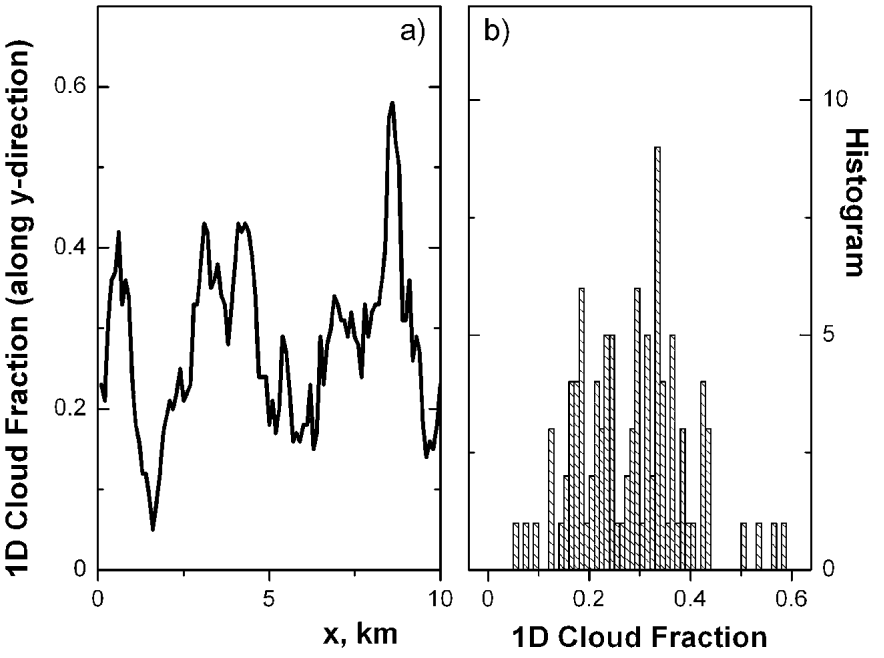

FIG. 5. (a) Realization and (b) corresponding histogram of 1D cloud fraction obtained for the LES cloud field (Fig. 3a).

sidered 1D lines is 100. Therefore, the probability of selecting a single 1D line that provides 1D cloud fraction $N_{\text{nadir}}(0)$ closely related to the 2D cloud fraction $N_{\text{nadir,avr}}$ is only 13%. This is consistent with previously reported results obtained for simulated fair-weather cumuli (randomly distributed clouds) and a virtual aircraft (Berg and Stull 2002). Note, Berg and Stull (2002) have obtained empirical equations that relate errors in the measured cloud fraction to the averaging time (or leg length) and the cloud fraction. These equations can provide both some guidance for planning a field experiment and estimates of the error bounds.

This low probability is estimated for zenith-pointing observations with a small FOV. Since the FOV is small, a surface instrument is unable "to see" neighboring parts of a cloudy sky that are adjacent to the small observed area. Therefore, the zenith-pointing observations (such as by lidar or radar) lose information about 2D (horizontal) cloud structure. Consequently, $N_{\text{nadir}}(0)$ values depend on a cross section and often differ from $N_{\text{nadir,avr}}$ (Figs. 4a,b). As the FOV increases, a larger area above a surface instrument can be observed. As a result, any single observation or short-term average (such as 15 min) with a large FOV can provide a more reasonable estimation of the actual 2D cloud fraction $N_{\text{nadir,avr}}$. For example, $N_{\text{nadir}}(80)$ values differ slightly from $N_{\text{nadir,avr}}$ and depend weakly on a cross section (Figs. 4a,b). Therefore, any single observation of $N_{\text{nadir}}(80)$ (within ~15 min time window) bears a resemblance to the large domain ($\sim 10 \times 10$ km^2). The question arises, how to derive $N_{\text{nadir}}(\alpha)$ from hemispherical observations [from $N_{\text{hemisph}}(\alpha)$]?

From the definitions of $N_{\text{nadir}}(\alpha)$ and $N_{\text{hemisph}}(\alpha)$ [Eqs. (1) and (2)] one can conclude that there are two main reasons for the difference between these two functions. The first reason is the *observational conditions*: plane-parallel observations (from nadir) for $N_{\text{nadir}}(\alpha)$ and hemispherical ones (from surface) for $N_{\text{hemisph}}(\alpha)$. The second reason is the *3D cloud geometry*: $N_{\text{nadir}}(\alpha)$ is independent of vertical (e.g., cloud-base heights and cloud vertical extents) and horizontal (e.g., cloud chord lengths and clear-sky chord lengths) cloud structure, whereas $N_{\text{hemisph}}(\alpha)$ can be sensitive to it. Let us use the probability of a clear line of sight to illustrate this sensitivity. For some cloud models (with assumed spatial and size distributions of clouds and constant cloud-base height), analytical expressions of the probability of a clear line of sight can be obtained in terms of cloud shape (e.g., parallelepipeds, truncated cones, and anvils), the cloud aspect ratio (height to diameter), and the nadir-view cloud fraction (e.g., Titov 1990; Killen and Ellingson 1994). For these models, the probability of a clear line of sight is a mostly decreasing function of zenith-viewing angle, and the rate of decrease of this probability depends on the vertical extent and structure of the clouds. However, for real broken clouds of highly variable cloud-base height, vertical extent, and irregular shape, this relationship is more complicated and perhaps entirely intractable. The 3D cloud geometry can be described by several different parameters; the cloud aspect ratio is the most important of them (Wielicki and Welch 1986; Malvagi et al. 1993; Benner and Curry 1998). We apply this widely used parameter to describe the 3D geometry of cloud fields.

Below we consider the effect of these *observational conditions* and the *cloud aspect ratio* (or 3D cloud geometry) on the difference between $N_{\text{nadir}}(\alpha)$ and $N_{\text{hemisph}}(\alpha)$.

To estimate the effect of the *observational conditions* only, we perform Monte Carlo simulations assuming that the cloud aspect ratio, γ, is very small. We obtain the third additional set of 3D cloud fields from the first (original) set by reducing the vertical size of each pixel by factor of 100. As a result, the domain-averaged vertical cloud size, H, is very small ($H \sim 0.001$ km) and $\gamma \sim 0.004$. In this case, the differences between $N_{\text{nadir}}(\alpha)$ and $N_{\text{hemisph}}(\alpha)$ are due to the observational conditions (Fig. 6a). There are substantial differences between $N_{\text{nadir}}(\alpha)$ and $N_{\text{hemisph}}(\alpha)$ for a large α only (Fig. 6a). Therefore, if the vertical cloud size is very small, then $N_{\text{hemisph}}(\alpha)$ can approximate $N_{\text{nadir}}(\alpha)$ quite accurately for $\alpha \leq 60$ (Fig. 6a).

To estimate the combined effect of both the *observation conditions* and the *cloud aspect ratio*, we compare $N_{\text{nadir}}(\alpha)$ and $N_{\text{hemisph}}(\alpha)$ obtained for the first (original) set (Fig. 6b). The domain-averaged vertical cloud size is $H \sim 0.1$ km and $\gamma \sim 0.4$ for this set. By comparing Fig. 6a with Fig. 6b, one can conclude that when the cloud aspect ratio grows, $N_{\text{hemisph}}(\alpha)$ increases and differences between $N_{\text{nadir}}(\alpha)$ and $N_{\text{hemisph}}(\alpha)$ can be magnified as well (Figs. 6a,b). Also, $N_{\text{hemisph}}(\alpha)$ is always equal to or larger than $N_{\text{nadir}}(\alpha)$.

The time-averaged (over 15-min sample) functions $N_{\text{hemisph}}(\alpha)$ and $N_{\text{nadir}}(\alpha)$ can be close to each other, but it does not mean that the same is true for their temporal realizations. For example, $N_{\text{hemisph}}(\alpha^*)$ approximates $N_{\text{nadir}}(\alpha^*)$ quite accurately for cross section 2 (Fig. 6a). However, the temporal realizations of $N_{\text{hemisph}}(\alpha^*)$ and $N_{\text{nadir}}(\alpha^*)$ are very different (Fig. 7): $N_{\text{nadir}}(\alpha^*)$ is almost "flat"; in contrast, $N_{\text{hemisph}}(\alpha^*)$ shows clearly defined peaks and valleys. Averaging a frequently sampled time series of $N_{\text{hemisph}}(\alpha)$ and $N_{\text{nadir}}(\alpha)$ allows one to decrease substantially the difference between time-averaged values of these two functions (Fig. 6a).

The weak time dependence of $N_{\text{nadir}}(\alpha^*)$ can be explained as follows. For given cloud fields ($H_b \sim 0.7$ km) and observation conditions ($\alpha = \alpha^*$), the radius of projection of the FOV (with the cone zenith angle 2α) onto the horizontal surface at height H_b, $R(\alpha)$, is about 4 km. Therefore, $N_{\text{nadir}}(\alpha^*)$ is obtained for a large area ($\sim 8 \times 8$ km^2) (Figs. 8a,b) for each time step. These large areas (shifted in the y directions) tend to have similar statistics. Obviously, $N_{\text{nadir}}(\alpha^*)$ does not significantly depend on the location of individual clouds within these areas. Conversely, $N_{\text{hemisph}}(\alpha^*)$ depends strongly on the cloud positions within the FOV (Figs. 8c,d). As a result, the peak in the $N_{\text{hemisph}}(\alpha^*)$ realization (Fig. 7) is caused by clouds located close to the center of the FOV (Figs. 8b,d), while the valley (Fig. 7) is due to clouds observed close to the edge of the FOV (Figs. 8a,c).

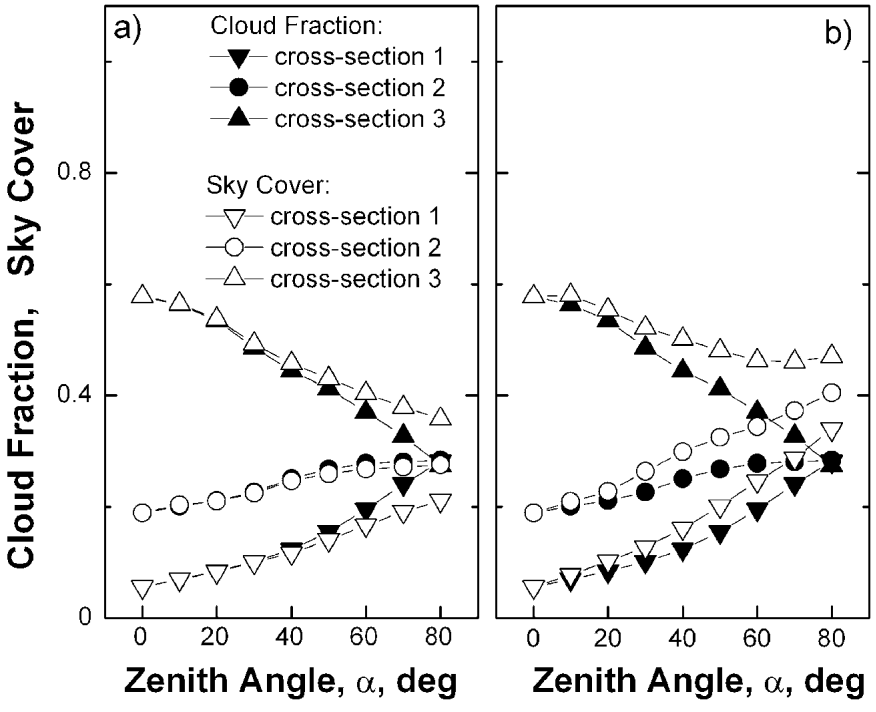

FIG. 6. Nadir-view cloud fraction and fractional sky cover obtained for (a) the third set of cloud fields produced by LES simulation and (b) the first set. The only difference between these two sets is the vertical size of clouds. The mean vertical cloud sizes are 0.0011 (the third set) and 0.11 km (the first set), corresponding to cloud aspect ratios of (a) 0.0037 and (b) 0.37.

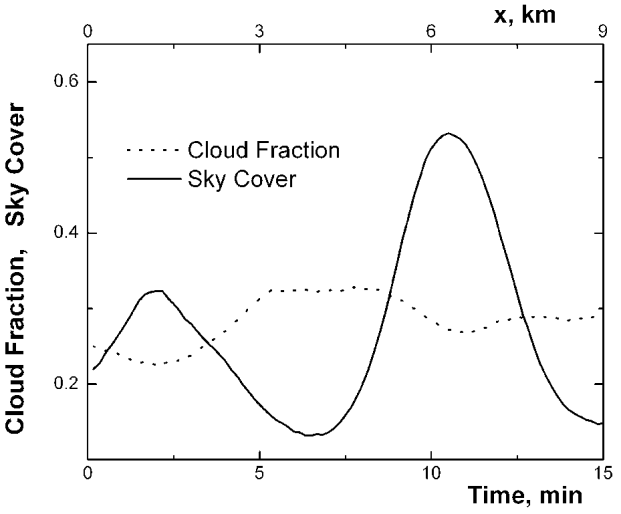

FIG. 7. Temporal realizations of nadir-view cloud fraction and fractional sky cover for cross section 2 ($x = 0.5$ km), FOV with cone zenith angle $2\alpha = 180°$, and $H \sim 0.001$ km. A scale converting time to equivalent distance is given at the top of the figure.

4. Correction of fractional sky cover

As noted above, the differences between $N_{\text{nadir}}(\alpha)$ and $N_{\text{hemisph}}(\alpha)$ are due to the *observation conditions* and the *cloud aspect ratio.* Therefore, the approximate equation that links $N_{\text{nadir}}(\alpha)$ and $N_{\text{hemisph}}(\alpha)$ should involve the cloud aspect ratio. Analysis of the LES simulation results shows that the relationship between $N_{\text{nadir}}(\alpha)$ and $N_{\text{hemisph}}(\alpha)$ can be described by

$$N_{\text{nadir}}(\alpha) \sim N^*_{\text{hemisph}}(\alpha) \quad \text{and} \tag{8}$$

$$N^*_{\text{hemisph}}(\alpha) = N_{\text{hemisph}}(\alpha)\left[1 - \gamma(0)\frac{\alpha}{\alpha^*}\right], \tag{9}$$

where $\gamma(0)$ is the cloud aspect ratio ($\alpha = 0$); $\gamma(0) = H(0)/D(0)$, where $H(0)$ and $D(0)$ are the temporal means of the vertical and horizontal cloud sizes, respectively. Here, $N^*_{\text{hemisph}}(\alpha)$ can be considered to be a *corrected* version of $N_{\text{hemisph}}(\alpha)$. Recall that temporal averaging is performed over 15 min of sampling. Here, we use the mean value of cloud chord length as the mean horizontal cloud size $D(0)$. The cloud chord length is defined as the distance between the trailing and leading edges of a cloud for a given wind direction (here, in the y direction). Note both the effective cloud diameter, defined as a circle of area equal to the area of this cloud [number of cloud pixels multiplied by the pixel area; Wielicki and Welch (1986)], and the mean cloud chord length (Malvagi et al. 1993) are frequently used as the characteristic horizontal cloud dimension. These two horizontal characteristics are not necessarily the same. In contrast to the effective cloud diameter, the cloud chord length along the wind direction can be determined from ground-based zenith-pointing instruments (e.g., lidar, radar).

Let us discuss Eq. (9). First, we assume implicitly that $H(0)$ and $D(0)$ can be representative for the large area. Previously we have demonstrated that the mean vertical cloud sizes of small marine cumulus clouds depend weakly on both the spatial sample size ($\sim 30 \times 30$ km^2) and the sample cloud fraction (Kassianov et al. 2003). Conceivably this may be valid for other cloud types. Second, $N_{\text{hemisph}}(\alpha)$ is measured directly by the TSI, and the cloud aspect ratio $\gamma(0)$ can be derived from collocated and coincident observations of a zenith-pointing lidar/radar. Note that surface observations at ARM sites provide a means for such retrieval (e.g., Clothiaux et al. 1999, 2000). Third, Eq. (9) gives exact results for a completely overcast cloud field [in this case $D(0) \gg H(0)$, and $\gamma(0) \sim 0$] and clear-sky conditions. Probably, the cloud aspect ratio could be estimated from TSI observations by using both small FOV (cloud bases are mostly seen) and large FOV (both cloud bases and sides can be seen) observations of sky cover. Since the same instrument would be used to estimate two essential parameters (the cloud fraction and the cloud aspect ratio), this kind of future study is important.

The next example illustrates the application of Eq. (9). Values of $\gamma(0)$ obtained for three different cross sections (Table 1) are used to define the corresponding $N^*_{\text{hemisph}}(\alpha)$ functions (Fig. 9). One can readily see that $N^*_{\text{hemisph}}(\alpha)$ matches $N_{\text{nadir}}(\alpha)$ closely for $\alpha \leq 60$ (Fig. 9). This good agreement is attributed to the following two main reasons. First, the 15-min average $N_{\text{hemisph}}(\alpha)$ itself approximates $N_{\text{nadir}}(\alpha)$ reasonably well if $\alpha \leq 60$ and the mean vertical cloud size is small (e.g., Fig. 6a). Second, $N^*_{\text{hemisph}}(\alpha)$ accounts for the mean vertical cloud size, $H(0)$, and $H(0)$ can be representative for the circle with radius $R(\alpha)$, where $\alpha \leq 60$. The large differences for cross section 1 and $\alpha > 60$ can be explained as follows. For cross section 1, the temporal mean value of $N_{\text{nadir}}(0)$ is very small (Fig. 9a); therefore, only a few cloud pixels have been used to estimate $H(0)$ and $D(0)$, and, consequently, $\gamma(0)$. Certainly, these estimations are not representative for large areas [circles with a radius of $R(\alpha)$, where $\alpha > 60$]. From Fig. 9, we can conclude that, given representative $\gamma(0)$, the correction of the fractional sky cover [see Eq. (9)] allows one to approximate the nadir-view cloud fraction quite accurately.

Since the cloud aspect ratio is quite low (~ 0.1) for both stratus and stratocumulus clouds, there is no need to use this correction for them. For cumulus clouds, the vertical and horizontal sizes are comparable (e.g., Benner and Curry 1998) and the cloud aspect ratio is relatively large (~ 1). Therefore, this correction should be useful for cumulus clouds. The latter frequently occur over the ocean in tropical and subtropical areas (e.g., Warren et al. 1988; Wielicki and Welch 1986).

We emphasize that Eq. (9) contains two time-averaged parameters [$N_{\text{hemisph}}(\alpha)$ and $\gamma(0)$] that char-

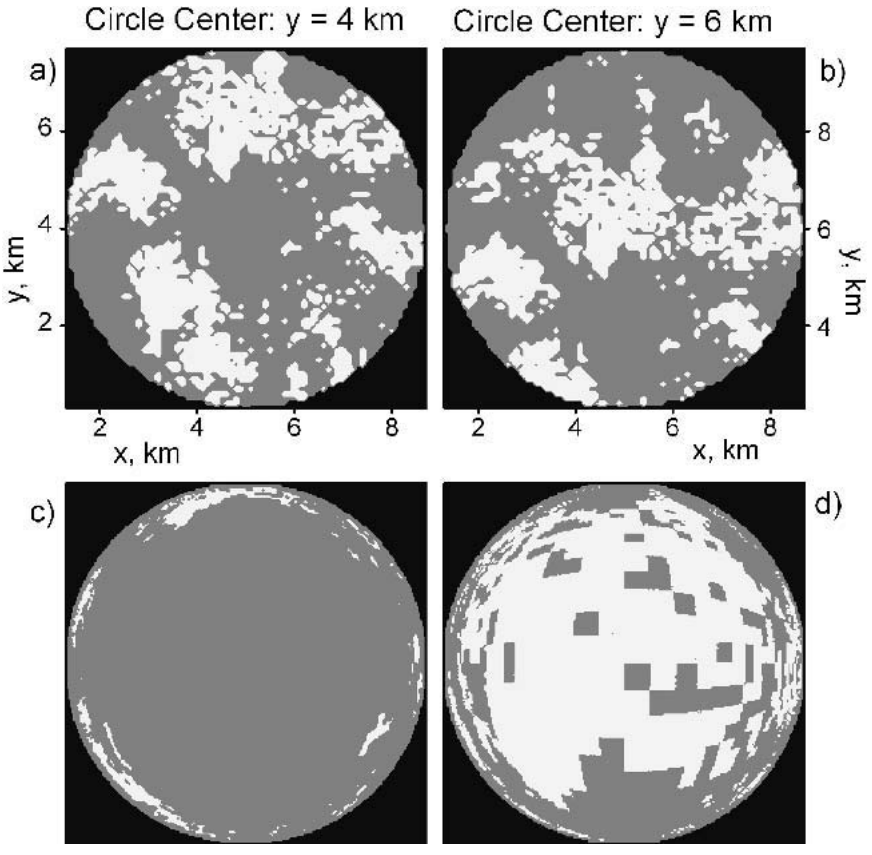

FIG. 8. Images of (a), (b) nadir-view cloud fraction and (c), (d) fractional sky cover for (b), (d) the peak and (a), (c) the valley as is shown in Fig. 7. These images correspond to an FOV with cone zenith angle $2\alpha = 180°$ and cloud-base height $H_b = 0.66$ km.

acterize 3D cloud geometry. These two parameters depend (indirectly and in a complex way) on the horizontal and the vertical variability of clouds (e.g., fluctuations of their horizontal cross section and the vertical extent). Since only a single field/realization of 3D cumulus clouds (Figs. 2, 3) is used to obtain this formula, its feasibility could be limited. More simulations of different cloud types are needed to provide a better understanding of the appropriateness and the accuracy of such a correction. Probably, a set of similar equations could be applied for different cloud types. To identify routinely cumulus clouds (and other cloud types) from TSI observations, one can use the standard deviation of the sky cover derived for a 15-min moving window and limited FOV (~100°): large values of this standard deviation correspond to the cumulus clouds. Note, the standard deviation of irradiance over a 21-min window (along with the ratio of average irradiance relative to clear-sky irradiance) is used successfully for estimating cloud type from surface pyranometer observations (Duchon and O'Malley 1999).

5. Cloudiness intercomparison IOP analysis

The above results (sections 3, 4) and analysis are aimed at determining the relationship between fractional sky cover and nadir-view cloud fraction. The cloud fields used in the study were produced by an LES model in an attempt to simulate real cloud fields as much as possible. Some of the conclusions confirmed previous results that an "instantaneous" comparison of hemispheric-view sky cover often does not relate well to a nadir-view cloud fraction. However, the primary purpose of the above study is to test the hypothesis that 15-min averages of frequently sampled (in this case every 30 s) sky cover relates much better to nadir-view cloud fraction, especially for some limited FOV (with the cone zenith angle 2α) of the simulated sky images.

The results in sections 3 and 4, while indicative, must be considered untested by the reality of the complexity

TABLE 1. The mean vertical, $H(0)$, and horizontal, $D(0)$, sizes of clouds and the corresponding cloud aspect ratio $\gamma(0)$ for three different cross sections and the whole domain (10 km × 10 km).

	Mean vertical cloud size (km)	Mean horizontal cloud size (km)	Cloud aspect ratio
Cross section 1	0.059	0.125	0.480
Cross section 2	0.085	0.425	0.200
Cross section 3	0.116	0.400	0.290
Domain averaged	0.112	0.300	0.373

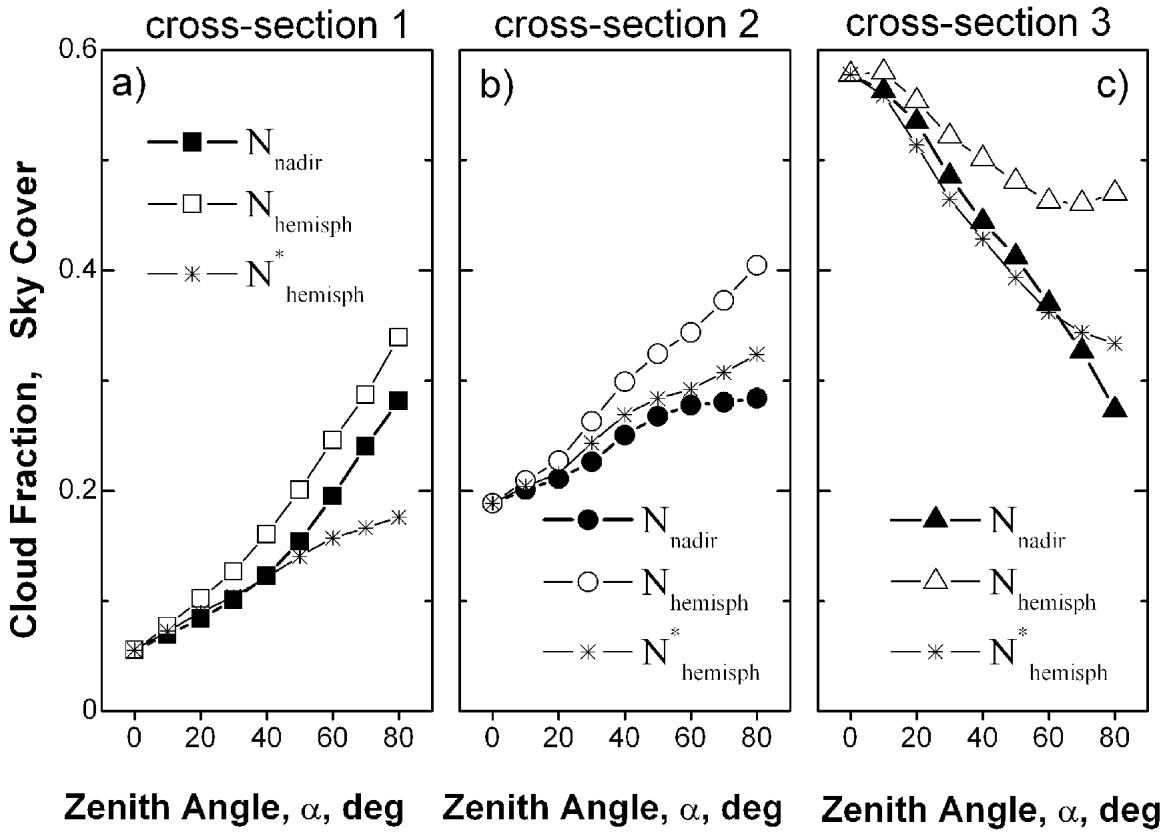

FIG. 9. The nadir-view cloud fraction, $N_{\text{nadir}}(\alpha)$, fractional sky cover $N_{\text{hemisph}}(\alpha)$, and *corrected* fractional sky cover $N^*_{\text{hemisph}}(\alpha)$ obtained for different cross sections.

of cloudiness often experienced in the field. To test these results with real cloudiness, we fielded a TSI (Long et al. 1999; Long et al. 2003) during the ARM Cloudiness Intercomparison IOP held at the ARM site in Oklahoma. This field experiment ran from 20 February through 6 May 2003, providing samples of many variations and types of cloudiness, including multilayer occurrences.

During the ARM Cloudiness Intercomparison IOP, lidar/radar observations accompanied the hemispherical TSI observations. Results of these active remote sensing instruments provide important information related to the spatial and temporal variability of clouds. Analysis of these results allows one to conclude that for the majority of clouds during the IOP, the mean horizontal cloud size is approximately an order of magnitude larger than the mean vertical cloud size. Therefore, on average, the observed clouds have a relatively low cloud aspect ratio (~0.1). As a result, we can expect weak dependence of the fractional sky cover on the FOV [see Eqs. (8) and (9)]. The model results also suggest that in this case the overall average sky cover value should increase noticeably for FOVs greater than 90° or 100°.

We process the sky images from the IOP for varying FOVs centered on zenith and ranging from 40° through 160° in diameter. For clear-sky and complete overcast, all FOVs will agree. Thus we select a subset of 36 days of the experiment that exhibit a wide range of cloudiness other than clear and overcast skies. Figure 10a shows the segment of realization of the sky cover obtained for three different FOVs. As the FOV increases, the TSI can see a larger area of cloudy atmosphere. As a result, increasing the FOV smoothes out the realization of the sky cover (Fig. 10a) and raises the time scale of the averaged autocorrelation function (Fig. 10b). The latter is obtained for a selected 36 cloudy days of the IOP and 1-h temporal window: within this window the temporal statistics of the sky cover do not change significantly. We define the decorrelation time scale (which is related to the temporal scale of N_{hemisph} fluctuations) as the time difference (ΔT) where the value of the autocorrelation function drops to zero. Note the autocorrelation function provides a measure of how closely $N_{\text{hemisph}}(\alpha; T)$ and $N_{\text{hemisph}}(\alpha; T + \Delta T)$ are related. One can see (Fig. 10b) that the decorrelation time scale is about 15 min and depends weakly on the FOV. The probability distribution function (PDF) of the autocorrelation function (at $\Delta T = 15$ min) is more sensitive to the FOV and may vary over a relatively narrow range (Fig. 10c). To obtain temporal statistics of fractional sky cover, we choose a 15-min window. The window width provides a reasonable balance between

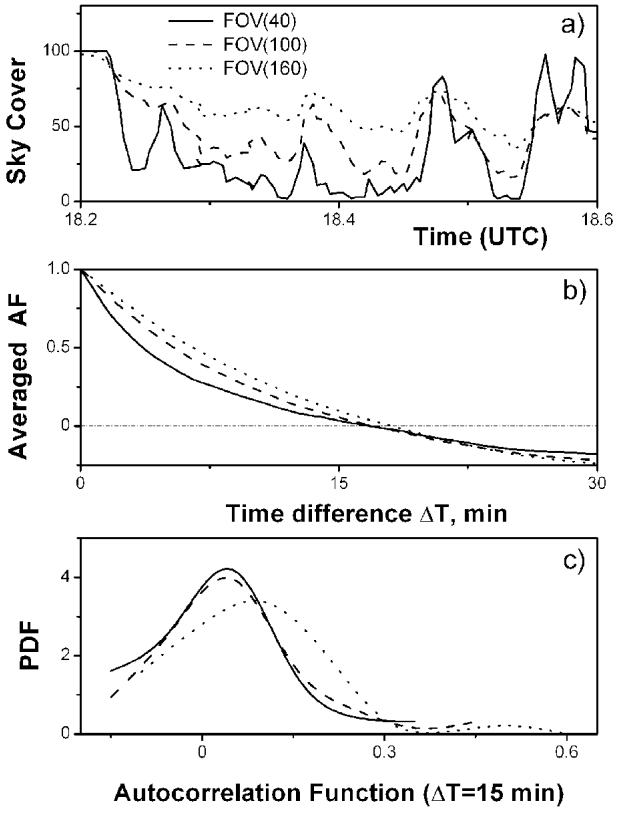

FIG. 10. (a) A fragment of the realization of the sky cover (22 Feb 2003), (b) the averaged autocorrelation function, and (c) the PDF of the autocorrelation function (at $\Delta T = 15$ min) obtained for three different FOVs: $2\alpha = 40°$ (solid line), $2\alpha = 100°$ (dashed line), and $2\alpha = 160°$ (dotted line).

the necessities of avoiding problems associated with cloud field nonstationarity and the small sampling size.

Figure 11 shows the overall average of the TSI sky cover by FOV with the cone zenith angle 2α. As hypothesized, the case study average of the total sky cover value remains at about the same magnitude (55%) for FOVs from 40° through 100°. But the value then increases with increasing FOV for 120°–160° FOVs. The TSI not only retrieves estimates of total sky cover, but also estimates what portion of the total is made up of "thin" or "opaque" clouds (Long et al. 2003; Pfister et al. 2003). We note that the increase in sky cover with increasing FOV is fundamentally a function of the opaque cloudiness, as the thin retrievals show no correlation with the FOV. This is expected in that most "thin" cloudiness has a low aspect ratio from the point of view of the imager, and most of the difference between sky cover and nadir cloud fraction is driven by cloud field aspect ratio effects.

This is further illustrated by a comparison between the 60° 15-min averages of sky cover to the corresponding 120° and 160° retrievals (Fig. 12). The three FOV 15-min averages tend to agree toward the greater sky cover (overcast) end of the spectrum; however, the

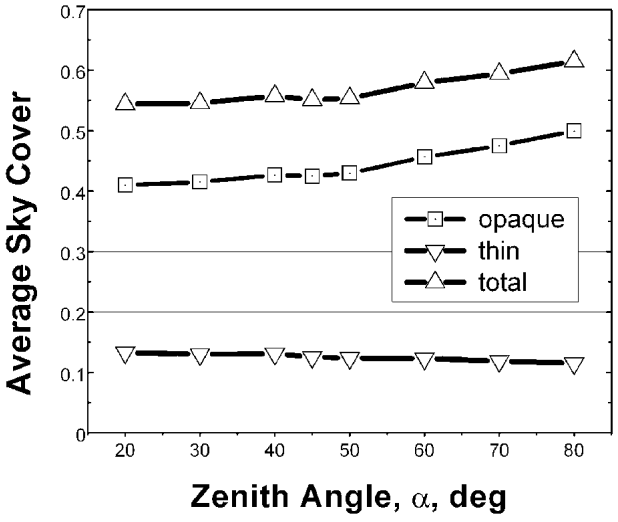

FIG. 11. Average sky cover as function of the cone zenith angle α (or FOV) for total, opaque, and thin cloudiness retrievals.

greater FOV shows a bias in the fitted lines toward the smaller sky cover end of the spectrum. This result comes about as a function of the wider FOV encompassing more of the sky, so that the probability is greater for detecting some cloudiness during the 15 min in an unevenly distributed cloud field. Also, as the view tends toward the horizon, the line of sight is more likely to encounter a cloud than an overhead view; that is, the "gaps" between the clouds become obscured by other clouds on the more slanted path through the cloud field.

For the narrower FOV, the view contains less of the slant-path effect. Additionally the narrower zenith-centered view "sees" more of the cloud bases and less of the cloud sides. Thus, the cloud aspect ratio exhibits

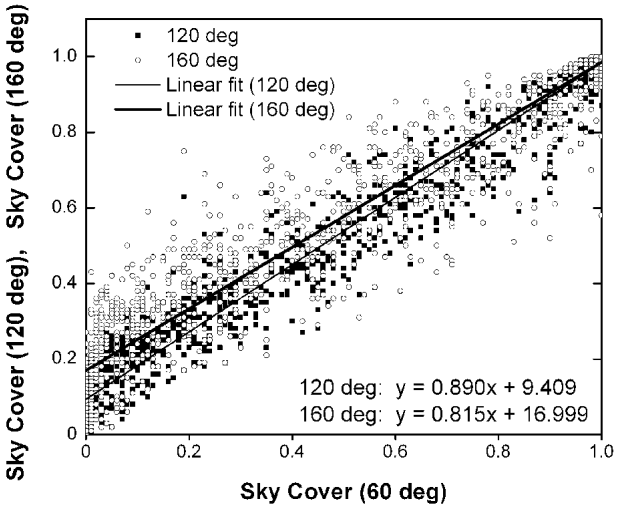

FIG. 12. Sky cover (15-min average) comparison among 60° FOV, 120° (black squares), and 160° (open circles) FOVs. The thin solid line is an rms fit to the 120° data; the thick solid line is for the 160° data.

far less effect on the 15-min average results for the narower FOV. As shown in Fig. 13, fitted lines compared in the smaller FOVs exhibit insignificant bias and offset. Thus it seems that 15-min averages of 30-s resolution, 100° FOV sky cover retrievals offer the best balance between a wide FOV and the corresponding larger coverage of cloud field; and they also produce results that are suitably related to the nadir cloud fraction as is needed for models.

6. Summary

The relationship between the nadir-view cloud fraction, N_{nadir}, and the hemispherical fractional sky cover, N_{hemisph}, is assessed using results of a large eddy simulation (LES) model and surface observations during the ARM Cloudiness Intercomparison IOP. Four-dimensional cloud fields (LES data) serve as input for the Monte Carlo simulations of temporal hemispherical observations of a total sky imager (TSI). We consider N_{nadir} and N_{hemisph} for different fields of view (FOVs) with cone zenith angle 2α. The main results are the following:

1) For given cloud fields (generated by an LES model), the effect of an individual cloud's evolution (local turbulence) on N_{nadir} and N_{hemisph} is relatively small for a 15-min temporal sample (the averaging period). Therefore, only a single cloud realization need be used for temporal TSI simulations (Taylor's frozen flow hypothesis). These realizations can be obtained from satellite retrievals and/or stochastic simulations.
2) There are two main reasons for the differences between N_{nadir} and N_{hemisph}. The first reason is the *observational conditions*: plane-parallel observations (from nadir) for N_{nadir} and hemispherical ones (from surface) for N_{hemisph}. The second reason is the *3D geometry of a cloud field*: N_{nadir} is independent of vertical–horizontal cloud structure; in contrast, N_{hemisph} can be sensitive to the vertical–horizontal cloud variability. The latter can be explained as follows. For a fixed horizontal cloud distribution (e.g., for a given N_{nadir}), the probability of a clear line of sight is a mostly decreasing function of zenith-viewing angle, and the rate of decrease of this probability depends on the vertical–horizontal cloud distribution.
3) The temporal averaging (15-min window) allows one to remove the effect of *observation conditions* (for $\alpha \leq 60$). Contrary to N_{nadir}, instantaneous N_{hemisph} is sensitive to the position of the clouds within the FOV and their vertical structure. However, an average from high temporal resolution samples of N_{nadir} and N_{hemisph} greatly decreases this difference. If cloud aspect ratio, γ, is relatively low ($\gamma \sim 0.1$ or less), the 15-min averages of N_{nadir} and N_{hemisph} are closely related (the effect of the *3D cloud geometry* is weak). For moderate and large γ values ($\gamma \geq 0.5$), the 15-min averages of N_{nadir} and N_{hemisph} can diverge considerably (the effect of the *3D cloud geometry* is strong).
4) Including the cloud aspect ratio, γ, makes it possible to overcome the effect of the 3D cloud geometry (for $\alpha \leq 60$). We suggest a correction of N_{hemisph} that incorporates the cloud aspect ratio and combines advantages of both the hemispherical TSI measurements (large area is observed) and the zenith-pointing lidar/radar retrievals (frequently sampled cloud geometry). The cloud aspect ratio could also be derived from collocated and coincident satellite measurements or from a climatological database.
5) Analysis of results from the ARM Cloudiness Intercomparison IOP supports the findings obtained from our model simulations. In particular, we demonstrate that sky cover of "thin" clouds is almost independent of the FOV. Since thin clouds typically have a large horizontal extension and small vertical thickness, their cloud aspect ratio is very low, and this expected invariant behavior of the sky cover is in harmony with our model results. Also we obtain the autocorrelation function of sky cover N_{hemisph} and estimate its decorrelation time scale, which is related to the temporal scale of N_{hemisph} fluctuations. The average value of the decorrelation time scale is about 15 min and depends weakly on the FOV. The individual values of the autocorrelation function (at a time scale of 15 min) may vary over a relatively narrow range and fall mostly below 0.3.

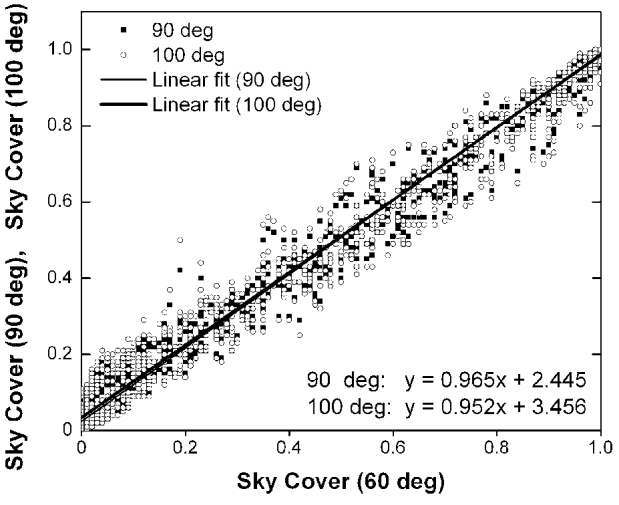

FIG. 13. Same as in Fig. 12 but for 90° and 100° FOV results.

The long-term dataset of sky cover (160° FOV) at different ARM sites is currently available. Our findings suggest that 15-min averages of 160° FOV fractional sky cover always overestimate the corresponding averages of nadir-view cloud fraction. Sometimes (for indi-

vidual instantaneous retrievals) such overestimation is substantial (more than 50%). For a relatively short averaging time (~15 min), the zenith-pointing observations with a narrow FOV (lidar/radar) can greatly (more than 100%) overestimate/underestimate the cloud fraction. These findings should be taken into account when the ground-based measurements are compared with satellite observations and model results. By using 100° FOV surface measurements, one can significantly (more than 2 times) decrease differences between derived values of the sky cover and the cloud fraction. These 100° FOV measurements provide a reasonable balance between the necessities of avoiding problems associated with zenith-pointing retrievals and the accuracy of N_{nadir} estimations.

An area worthy of further investigation is the derivation of the cloud aspect ratio from hemispherical TSI observations. Measurement of this important cloud parameter could be possible with both small FOV and large FOV estimations of sky cover. For small FOVs, cloud bases are mostly observed; for large FOVs, both cloud bases and sides can be seen. We plan to address this issue and compare the derived cloud aspect ratios with those obtained by independent measurements (surface and satellite).

Acknowledgments. This work was supported by the Office of Biological and Environmental Research of the U.S. Department of Energy as part of the Atmospheric Radiation Measurement Program. We thank the anonymous reviewers for their constructive comments, which improved the paper. We are grateful to N. Burleigh for assistance during the preparation of the manuscript.

REFERENCES

Barker, H., 1996: Estimating cloud field albedo using one-dimensional series of optical depth. *J. Atmos. Sci.,* **53,** 2826–2837.

Benner, T., and J. Curry, 1998: Characteristics of small tropical cumulus clouds and their impact on the environment. *J. Geophys. Res.,* **103,** 28 753–28 767.

Berg, L., and R. Stull, 2002: Accuracy of point and line measures of boundary layer cloud amount. *J. Appl. Meteor.,* **41,** 640–650.

Christian, T., and R. Wakimoto, 1989: The relationship between radar reflectivities and clouds associated with horizontal roll convection on 8 August 1982. *Mon. Wea. Rev.,* **117,** 1530–1544.

Clothiaux, E., and Coauthors, 1999: The Atmospheric Radiation Measurement Program cloud radars: Operational modes. *J. Atmos. Sci.,* **56,** 819–827.

——, T. Ackerman, G. Mace, K. Moran, R. Marchand, M. Miller, and B. Martner, 2000: Objective determination of cloud heights and radar reflectivities using a combination of active remote sensors at the ARM CART sites. *J. Appl. Meteor.,* **39,** 645–665.

Del Genio, A. D., M. S. Yao, W. Kovari, and K. K. W. Lo, 1996: A prognostic cloud water parameterization for global climate models. *J. Climate,* **9,** 270–304.

Duchon, C. E., and M. S. O'Malley, 1999: Estimating cloud type from pyranometer observations. *J. Appl. Meteor.,* **38,** 132–141.

Fairall, C., and J. Hare, 1990: An eight-month sample of marine stratocumulus cloud fraction, albedo and integrated liquid water. *J. Climate,* **3,** 847–864.

Hahn, C., W. Rossow, and S. Warren, 2001: ISCCP cloud properties associated with standard cloud types identified in individual surface observation. *J. Climate,* **14,** 11–28.

Harshvardhan, D. A. Randall, and T. G. Corsetti, 1989: Earth radiation budget and cloudiness simulations with a general circulation model. *J. Atmos. Sci.,* **46,** 1922–1942.

Hogan, R., C. Jacob, and A. Illingworth, 2001: Comparison of ECMWF winter-season cloud fraction with radar-derived values. *J. Appl. Meteor.,* **40,** 513–525.

Kassianov, E., T. Ackerman, R. Marchand, and M. Ovtchinnikov, 2003: Satellite multiangle cumulus geometry retrieval: Case study. *J. Geophys. Res.,* **108,** 4117, doi:10.1029/2002JD002350.

Killen, R., and R. Ellingson, 1994: The effect of shape and spatial distribution of cumulus clouds on longwave irradiance. *J. Atmos. Sci.,* **51,** 2123–2136.

Lazarus, S., S. Krueger, and G. Mace, 2000: A cloud climatology of the Southern Great Plains ARM CART. *J. Climate,* **13,** 1762–1775.

Long, C., T. Ackerman, and J. DeLuisi, 1999: Estimation of fractional sky cover from broadband SW radiometer measurements. Preprints, *10th Conf. on Atmospheric Radiation,* Madison, WI, Amer. Meteor. Soc., 383–386.

——, D. Slater, and T. Tooman, cited 2003: Total Sky Imager (TSI) Model 880 status and testing results. Atmospheric Radiation Measurement Program Tech. Rep. ARM TR-004. [Available online at http://www.arm.gov/docs/documents/tech_reports/index.html.]

Mace, G., and S. Benson-Troth, 2002: Cloud-layer overlap characteristics derived from long-term cloud radar data. *J. Climate,* **15,** 2505–2515.

Malvagi, F., R. Byrne, G. Pomraning, and R. Somerville, 1993: Stochastic radiative transfer in a partially cloudy atmosphere. *J. Atmos. Sci.,* **50,** 2146–2158.

Minnis, P., 1989: Viewing zenith angle dependence of cloudiness determined from coincident GOES EAST and GOES WEST data. *J. Geophys. Res.,* **94,** 2303–2320.

Morcrette, J.-J., 1991: Evaluation of model-generated cloudiness: Satellite-observed and model-generated diurnal variability of brightness temperature. *Mon. Wea. Rev.,* **119,** 1205–1224.

Pfister, G., R. McKenzie, J. Liley, A. Thomas, B. Forgan, and C. Long, 2003: Cloud coverage based on all-sky imaging and its impact on surface solar irradiance. *J. Appl. Meteor.,* **42,** 1421–1434.

Randall, D., J. Coakley Jr., C. Fairall, R. Kropfli, and D. Lenschow, 1984: Outlook for research on subtropical marine stratiform clouds. *Bull. Amer. Meteor. Soc.,* **65,** 1290–1301.

Rodts, S., P. Duynkerke, and H. Jonker, 2003: Size distributions and dynamical properties of shallow cumulus clouds from aircraft observations and satellite data. *J. Atmos. Sci.,* **60,** 1895–1912.

Rossow, W., A. Walker, and L. Garder, 1993: Comparison of ISCCP and other cloud amounts. *J. Climate,* **6,** 2394–2418.

Russ, J. C., 1986: *Practical Stereology.* Plenum Press, 185 pp.

Stoyan, D., and H. Stoyan, 1994: *Fractals, Random Shapes and Point Fields.* John Wiley and Sons, 389 pp.

Titov, G., 1990: Statistical description of radiation transfer in clouds. *J. Atmos. Sci.,* **47,** 24–38.

Warren, S., C. Hahn, J. London, R. Chervin, and R. Jenne, 1988: Global distribution of total cloud cover and cloud type amounts over the ocean. NCAR Tech. Note NCAR/TN-317+STR, 41 pp. plus 170 maps.

Wielicki, B., and R. Welch, 1986: Cumulus cloud properties derived using Landsat satellite data. *J. Climate Appl. Meteor.,* **25,** 261–276.

Wood, R., and P. Field, 2000: Relationships between total water, condensed water, and cloud fraction in stratiform clouds examined using aircraft data. *J. Atmos. Sci.,* **57,** 1888–1905.